


High-Speed Efficient On-Chip Electro-Optic Modulator Based on Midinfrared Hyperbolic Metamaterials

Dongdong Li,^{1,2,3} Hongbin Ma^{1,2,3}, Qiwei Zhan^{1,2,3}, Jie Liao^{1,2,3}, Wen-Yan Yin,^{1,2,3,*}
Hongsheng Chen,^{1,2,3,†} and Haoliang Qian^{1,2,3,‡}

¹*Interdisciplinary Center for Quantum Information, State Key Laboratory of Modern Optical Instrumentation, College of Information Science and Electronic Engineering, Zhejiang University, Hangzhou 310027, China*

²*ZJU-Hangzhou Global Science and Technology Innovation Center, Key Laboratory of Advanced Micro/Nano Electronic Devices & Smart Systems of Zhejiang, Zhejiang University, Hangzhou 310027, China*

³*International Joint Innovation Center, ZJU-UIUC Institute, Zhejiang University, Haining 314400, China*

 (Received 4 April 2021; revised 6 July 2021; accepted 12 August 2021; published 1 September 2021)

Integrated modulators are key components for on-chip optical communication and information processing, which have become leading technologies in the current information-growth era. Hence, high-speed, efficient, and compact integrated modulators are in high demand. However, the current integrated midinfrared modulators meet these requirements with difficulty. Here, we present a high-speed and efficient on-chip electro-optic modulator based on midinfrared hyperbolic metamaterials using stacking of graphene and hexagonal boron nitride. The length of the modulation region is only 60 nm, which is integrated on a plasmonic waveguide composed of hyperbolic metamaterials. The maximum modulation depth is up to 30 dB, and the 3-dB modulation speed can reach up to 50 GHz, which is supported by a detailed study of a small-signal frequency-response model. Our work provides an alternative scheme for the design of modulators with the requirements of sub-100-nm integration and 50-GHz modulation speed or even beyond, which can be directly implemented into a two-dimensional-materials-based photonic integrated circuits platform.

DOI: [10.1103/PhysRevApplied.16.034002](https://doi.org/10.1103/PhysRevApplied.16.034002)

I. INTRODUCTION

The midinfrared (MIR) region of the electromagnetic spectrum, especially wavelengths of 3–5 μm , has attracted much attention due to its unique applications, including chemical and biological sensing [1–4], free-space communication [1,5], defense technologies [6], and so on. With the exponential growth of data traffic, on-chip communication and information processing are becoming the leading technologies in the current information-growth era. Efficient, compact, and low-power on-chip parametric processors are in demand. Consequently, it is important and urgent to realize a MIR photonic integrated circuits (PICs) platform. In recent years, MIR technologies have been advancing rapidly, and many integrated MIR devices have been developed, such as on-chip MIR sources [7–9], photoelectric detectors [10], sensors [11], frequency combs [12,13], bolometers [14], etc. However, most current MIR systems are assemblages of discrete components

and there have been few researches reporting high-speed and efficient on-chip MIR electro-optic (EO) modulators.

An optical modulator is one of the most crucial components in a PICs platform, which typically determines the performance of the whole integrated system, including operation bandwidth, system loss, and dynamic range [15]. Due to the lack of suitable EO materials, the development of MIR modulators has always been a bottleneck. An implementation scheme of the existing technology includes an acousto-optic modulator based on acousto-optic materials [16,17], such as GaP, Ge, GaAs, etc. However, such a device is bulky and low speed, which cannot meet the requirements for on-chip integration applications. As an alternative, an integrated MIR waveguide modulator composed of silicon on lithium niobate has been reported [18] based on the Pockels effect, which still has a relatively large size with millimeter-scale length. Two-dimensional (2D) materials also provide notable opportunities for designing conceptual optoelectronic devices. A MIR EO modulator in few-layer black phosphorus has been demonstrated using the quantum confined Franz-Keldysh effect [19]. However, practical applications may be limited because of the operating voltage of up to 150 V. Graphene is considered to be one of the best candidates

*wyyin@zju.edu.cn

†hansomchen@zju.edu.cn

‡haoliangqian@zju.edu.cn

among the 2D materials due to its easy integration features [20], extraordinary electrical transport properties [21], and strong light-matter interactions [22]. An electrically controlled MIR modulator with broadband wavelength range and high-speed response has been reported using a metasurface composed of optical antennas on graphene [23]. Nevertheless, intending to meet the exponential growth of Big Data and practical requirements for integrated photonics and interconnection applications, there is still an urgent requisite for performance improvement, especially in terms of nanoscale compactness and modulation speed.

Here, we propose a high-speed, efficient, and compact MIR modulator based on hyperbolic metamaterials (HMMs) using stacking of graphene and hexagonal boron nitride (*h*-BN). The high-speed operation is enabled by ultrafast EO response from graphene. The efficient modulation depth is attributed to the large tunable phase transition owing to the good anisotropic properties from the HMM design. The compact integration is based on the strong light-matter interaction ascribed to the HMM based on 2D material stackings (HMM2Ds), as well as the low-loss plasmonic air-gap waveguide design. The proposed MIR modulator using HMM2Ds can be directly implemented into a 2D-material-based PICs platform, as well as other photonic systems including silicon photonic systems, which brings the PICs platform one step closer to reality.

II. DESIGN PRINCIPLES AND DEVICE CONFIGURATION

Several key advantages make HMM2Ds an excellent combination. To begin with, the combination of HMM2Ds with van der Waals heterostructures can be assembled in the required geometries without the typical restraint of interfacial lattice matching. And then, layered *h*-BN with a hexagonal lattice is an atomically flat wide-gap insulator with minimal charged impurities, which can enhance the quality of electronic properties for graphene devices [24,25]. Moreover, the optical properties of graphene can be tuned extensively through electrostatic or chemical doping.

However, a HMM assembled with metal and dielectric has relatively high loss, and thus cannot be directly used for a waveguide-based optical modulator. Here, we implement such HMM2Ds into a plasmonic gap-mode waveguide design enabling low loss and compact integration. The plasmonic air-gap mode is supported by planar waveguide structure formed by anisotropic type-II HMM2Ds. As shown in Fig. 1, the integrated device is composed of five segments, namely two signal propagation regions, two modulation regions, and one buffer region. When the chemical potential of graphene is adjusted by electrical doping, the HMM2Ds will experience different HMM types (phase transition) and optical properties of modulation regions will be changed correspondingly, causing

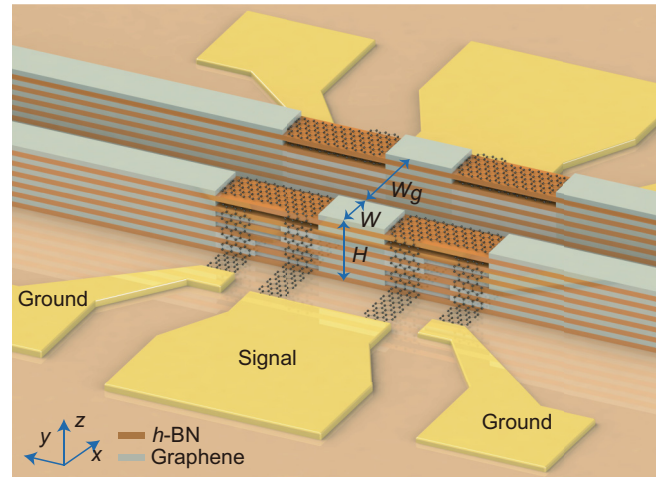


FIG. 1. Schematic depiction of the proposed integrated planar waveguide modulator on quartz substrate. It is composed of five segments, namely signal propagation region, modulation region, buffer region, modulation region, and signal propagation region in turn. W and H are the width and thickness of HMM2Ds, respectively. W_g is the width of the air gap. The chemical potential of the graphene layer in modulation regions can be tuned by applied voltage supported by graphene nanoribbons. In order to obtain different voltages for different graphene layers, L-type graphene is stacked alternately (see Sec. S1 of the Supplemental Material for details [26]). Note that the graphene layers between each region are separated for electrical insulation. Here, only the top two layers of graphene in modulation regions are depicted as the latticelike atomic-structure diagram, while the rest are represented by slabs. The total number of pairs for HMM2Ds depends on the thickness H , and only a few pairs are presented here as representative.

the destruction of plasmonic air-gap modes. In an effort to increase the modulation depth, the modulation region is physically separated into two parts and a buffer region is introduced. The buffer region is exactly the same as the propagation region, which is deployed to create the additional phase-transition boundaries between the buffer region and first and second modulation regions. This can greatly improve the modulation depth without sacrificing modulation speed, as the total length of the modulation region is the same with and without the buffer region. Note that the high-speed ground-signal-ground electrodes are perfectly fitted for this configuration as shown in Fig. 1. The modulation regions, composed of multiple capacitive graphene-*h*-BN pairs contacted by graphene nanoribbons on the sides [27], are the crucial parts of the device, where holes and electrons are induced with the same mobility and density of states in different single-layer graphene sheets due to the symmetric conical band structure [21]. In this case, the same optical conductivity can be obtained in different graphene layers, and each graphene layer can contribute equally to MIR modulation.

III. THEORETICAL ANALYSIS OF THE HMM2Ds

The performance of modulators can be evaluated by several key figures of merit, such as operating bandwidth, insertion loss, modulation depth, and speed [20]. For the investigation of the allowed operating bandwidth, we calculate the effective permittivity of the proposed HMM2Ds at different frequencies. The optical conductivity of graphene sheet is derived from the Kubo formation [28]:

$$\sigma_g(\omega) = \frac{ie^2k_B T}{\pi\hbar^2(\omega+i\Gamma)} \left[\frac{\mu_c}{k_B T} + 2 \ln(e^{-\mu_c/k_B T} + 1) \right] + \frac{ie^2(\omega+i\Gamma)}{\pi\hbar^2} \int_0^\infty \frac{f(-E) - f(E)}{(\omega+i\Gamma)^2 - 4(E/\hbar)^2} dE, \quad (1)$$

where e is the charge of the electron, ω is the angular frequency, \hbar is the reduced Planck constant, $f(E) = 1/(e^{(E-\mu_c)/k_B T} + 1)$ is the Fermi-Dirac distribution function, E is the electron energy, k_B is the Boltzmann constant, μ_c is the chemical potential, and $\Gamma = 1/\tau$ with $\tau = 0.5$ ps representing the electron relaxation time in graphene [29]. Here, we set the working temperature as $T = 78$ K so as to extend the tuning range of the phase transition of HMM2Ds while such temperature can be easily accessed using liquid nitrogen. Also, it is worth noting that the temperature has little effect on the optical conductivity of highly doped graphene [30], especially for the temperature range including room temperature and 78 K. For

highly doped or gated graphene ($|\mu_c| \gg k_B T$), the chemical potential can be expressed as $\mu_c = \sqrt{\pi\hbar^2 v^2 n}$ [28], where $v = 10^6$ m/s is the Fermi velocity, $n = \epsilon_0 \epsilon_r U/d$ is the carrier density, ϵ_0 is the vacuum dielectric constant, $\epsilon_r = 3.29$ is the static out-of-plane dielectric constant, which is that of h -BN [31] in this work, U is the applied voltage, and d is the distance between adjacent graphene sheets. The permittivity tensor of h -BN is diagonal with $\epsilon_{xx,h\text{-BN}} = \epsilon_{yy,h\text{-BN}} = \epsilon_{\parallel,h\text{-BN}}$ and $\epsilon_{zz,h\text{-BN}} = \epsilon_{\perp,h\text{-BN}}$ being the in-plane and out-of-plane components, respectively, which can be described by a single Lorentzian [31–34]:

$$\epsilon_{\alpha,h\text{-BN}} = \epsilon_{\infty\alpha} \left[1 + \frac{(\omega_{\text{LO},\alpha})^2 - (\omega_{\text{TO},\alpha})^2}{(\omega_{\text{TO},\alpha})^2 - \omega^2 - i\omega\Gamma_\alpha} \right], \quad \alpha = \perp, \parallel, \quad (2)$$

where $\omega_{\text{TO},\perp} = 746$ cm^{-1} , $\omega_{\text{LO},\perp} = 819$ cm^{-1} , $\Gamma_\perp = 4$ cm^{-1} , $\epsilon_{\infty\perp} = 2.89$ for out of plane; and $\omega_{\text{TO},\parallel} = 1372$ cm^{-1} , $\omega_{\text{LO},\parallel} = 1610$ cm^{-1} , $\Gamma_\parallel = 5$ cm^{-1} , $\epsilon_{\infty\parallel} = 4.97$ for in plane. When the long-wavelength approximation is satisfied, the effective dielectric components of the proposed HMM2Ds can be calculated by the effective medium theory [35]:

$$\epsilon_{\parallel} = \rho\epsilon_g + (1 - \rho)\epsilon_{\parallel,h\text{-BN}}, \quad (3)$$

$$\frac{1}{\epsilon_{\perp}} = \frac{\rho}{\epsilon_g} + \frac{1 - \rho}{\epsilon_{\perp,h\text{-BN}}}, \quad (4)$$

where $\rho = t_g/(t_{h\text{-BN}} + t_g)$ is the filling fraction of graphene in HMM2Ds, $t_g = 0.335$ nm and $t_{h\text{-BN}} = 0.333$ nm

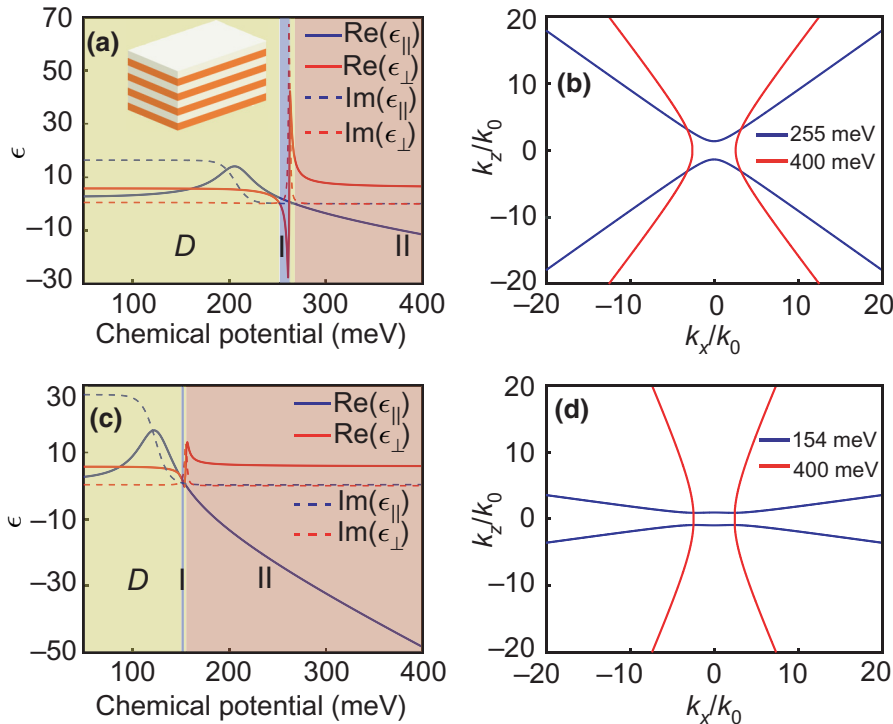


FIG. 2. The effective permittivity and isofrequency dispersion contours. The real and imaginary parts of effective permittivity tensors varying with chemical potential at (a) 3 μm and (c) 5 μm . ϵ_{\perp} and ϵ_{\parallel} denote the out-of-plane and in-plane components of effective permittivity tensors, respectively. The inset in (a) shows a schematic of HMM2Ds. D, dielectric; I, type I; II, type II. Isofrequency dispersion contours for different chemical potentials at fixed wavelengths of (b) 3 μm and (d) 5 μm . The blue line represents type I and the red line type II. Note that due to the influence of loss, the dispersion of the type-I isofrequency dispersion contour varies more slowly at 5 μm compared with that at 3 μm .

are the thickness of graphene and h -BN, respectively, and $\epsilon_g(\omega) = 1 + i\sigma_g(\omega)/\epsilon_0\omega t_g$ is the permittivity of graphene. In our case, $k_0 D = 2\pi D/\lambda_0 \rightarrow 0$, where $D = t_{h\text{-BN}} + t_g$ is the periodic thickness and k_0 is the free space wave number. The quasistatic limit is met, and the spatial dispersion effect can be safely neglected [36].

Figures 2(a) and 2(c) show the variation of effective permittivity with the chemical potential at wavelengths of 3 and 5 μm , respectively. Different HMM types can be realized and there exist fruitful phase transitions under different doping conditions, such as the transition from type II to type I. Such tunability would be also valid at the working wavelength between 3 and 5 μm as expected. Two normalized representative isofrequency dispersion contours at 3 and 5 μm are shown in Figs. 2(b) and 2(d), respectively.

IV. GEOMETRICAL OPTIMIZATION OF HMM2Ds

For the on-chip waveguide-based device, the system energy efficiency is highly related to the loss [20,37], and we quantify it by optical propagation loss. Figure 3 shows the geometrical size optimization of HMM2Ds at a wavelength of 5 μm when the chemical potential of graphene is 400 meV. The variations of propagation loss with total thickness H and width W of HMM2Ds are given in Figs. 3(a) and 3(b), respectively. As one can see clearly, there exist resonant modes at some values of thickness and width (such as $H = 147$ nm when $W = 600$ nm), which should be avoided during the HMM2D design due to the

very limited allowed propagation distance. Here, mode analysis is carried out by the finite-element method using COMSOL Multiphysics, and the imaginary part of the effective mode index is utilized to represent the propagation loss.

Aiming to show the differences between the resonant lossy mode and long-propagation mode, two representative electric field distributions are plotted in Figs. 3(c)–3(h). For the resonant lossy mode, all the electric field components (x , y , and z) are concentrated inside the HMM, featuring the high-order resonance mode. It is the hyperbolic polaritons that are guided within the HMM2Ds (see Sec. S2 of the Supplemental Material for details [26]), and the guided hyperbolic polariton modes in h -BN have been researched by Dolado *et al.* [38]. Contrarily, for the long-propagation mode, the electromagnetic field is mainly distributed inside the air gap, including the E_x and E_z components. Thus, the loss is greatly reduced (0.0376 dB/ μm). The long-propagation mode is beneficial to many integrated photonic applications such as waveguides, on-chip modulators, and so on. The resonant lossy mode is dominated by hyperbolic polariton mode, while the long-propagation mode is dominated by plasmonic air-gap mode. Although the structures in Figs. 3(f)–3(h) could also support the hyperbolic polariton mode, they have a much larger effective mode index, which can be easily skipped during the experiment with excitation engineering on the effective mode index (see Sec. S3 of the Supplemental Material for details [26]). It is worth noting

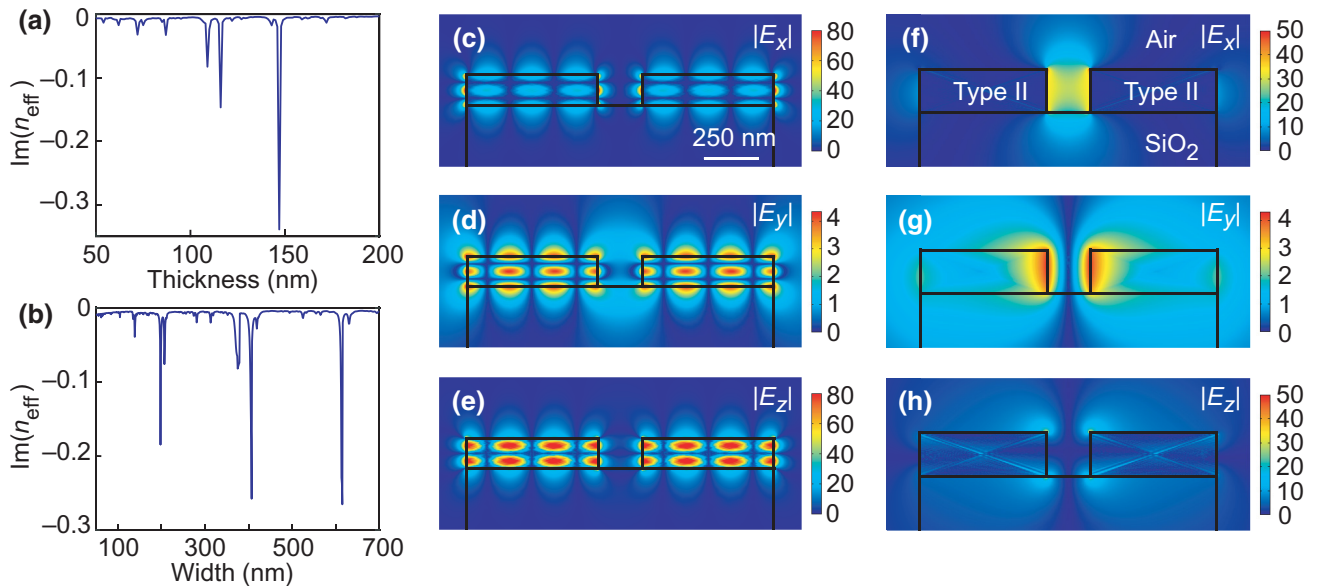


FIG. 3. The geometrical size optimization of HMM2Ds with air gap $W_g = 200$ nm at an operation wavelength of 5 μm . (a) The relationship between propagation loss and thickness of HMM2Ds when $W = 600$ nm. (b) The relationship between propagation loss and width of HMM2Ds when $H = 150$ nm. (c)–(e) The electric field strength distribution of different components for the resonant lossy mode with $H = 147$ and $W = 600$ nm, which is not preferred for the design of a low-loss modulator due to the very limited allowed propagation distance. (f)–(h) The electric field strength distribution of different components for the long-propagation mode with $H = 200$ and $W = 600$ nm. Here, the chemical potential of graphene is doped at 400 meV.

that once the graphene is modulated with external voltages, the HMM2Ds will encounter the phase-transition process, where the long-propagation plasmonic air-gap mode will no longer be supported, achieving the functionality of modulation.

V. MODULATION DEPTH AND SPEED ANALYSIS

For the majority of applications, such as high-data-rate interconnects and high-sensitivity sensing, a large modulation depth (>7 dB) is preferred [20,39]. The modulation depth is often characterized by the so-called extinction ratio in transmission-type devices, namely the ratio between the maximum and minimum transmittance. Here, based on the above anisotropic permittivity and mode study, the geometrical parameters $W = 225$ nm,

$H = 70$ nm, and $W_g = 300$ nm at a wavelength of $5 \mu\text{m}$ are chosen for modulation depth and speed analysis, with the propagation loss as 0.0844 dB/ μm . Figure 4(a) shows the calculated modulation depth as a function of the applied voltage V_a at the low-frequency limit, including the dc voltage V_{dc} and the small-signal modulation voltage V_C . There exists a region where the maximum modulation depth is up to 30 dB, which corresponds to an optimized modulation voltage V_C of -0.1342 mV. In this work, the modulation region is initially doped by V_{dc} at 0.9851 mV, which gives a chemical potential of 170 meV, while the signal propagation and buffer regions are chemically doped at 400 meV to minimize the propagation loss. Once the modulation voltage V_C is applied, the chemical potential of graphene will decrease resulting in the off state, as shown in the inset of Fig. 4(a).

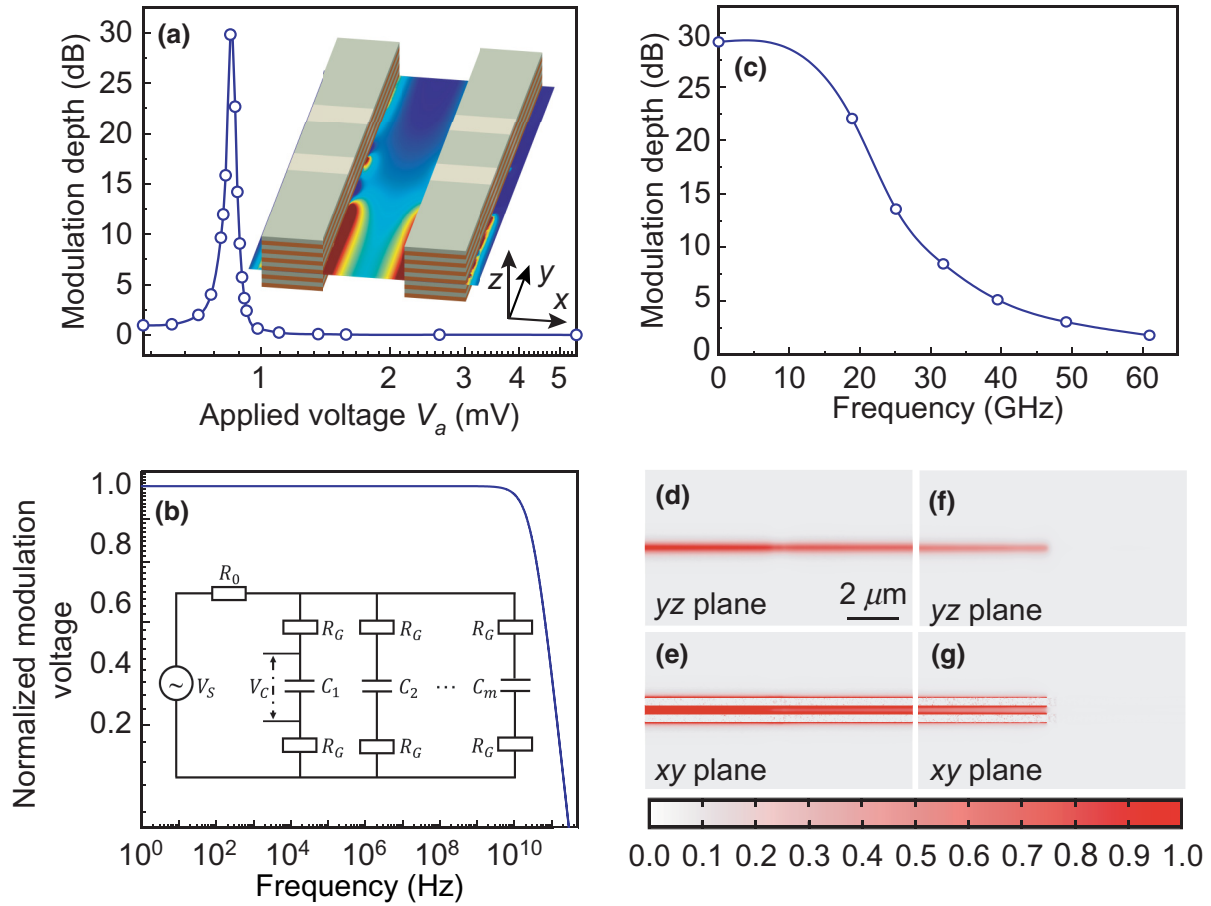


FIG. 4. Modulation depth and speed analysis based on the small-signal frequency-response model. (a) Modulation depth as a function of the applied voltage V_a . The modulation depth is defined as the energy ratio $10 \log_{10}(\text{on/off})$, where “on” means on state with maximum transmittance while “off” represents the opposite case. The inset shows one example of off-state modulation. (b) Normalized modulation voltage as a function of small-signal frequency. The inset shows the corresponding equivalent small-signal high-frequency circuit model of the proposed device. V_S represents the small-signal square wave voltage from the function generator. R_0 is the resistance of the function generator, which is typically 50Ω . R_G is the total resistance per graphene layer, including the internal resistance of graphene R_g with a sheet resistance of $40 \Omega/\text{sq}$ [40] and contact resistance of graphene-graphene nanoribbons R_{gg} (1000Ω) [27]. C_m is the capacitance of the m th graphene capacitor with value C_G and $2m$ is the number of doped graphene layers. (c) Modulation depth as a function of the small-signal frequency. (d)–(g) The energy flow distributions in yz and xy planes when the modulator is on and off, respectively. Note that the yz plane is cut in the center of the air gap while the xy plane is in the middle of the HMM waveguide.

With increasing small-signal frequency, the actual modulation voltage V_C decreases gradually, and the HMM2Ds will be incapable of achieving the off state. Thus, the modulation speed emerges as another key parameter to determine the performance, which is typically characterized by the frequency-dependent optical modulation depth at the operation wavelength. In general, the electrical properties of EO modulators can be accurately modeled by a network of distributed resistors (R) and capacitors (C). The inset in Fig. 4(b) shows the equivalent small-signal high-frequency circuit response model of the proposed device. The actual modulation voltage (V_C) applied on the device can be obtained from function generator $V_S[\text{sgn}(\sin(\omega t)) - 1]/2$ by the network of distributed resistors and capacitors as

$$V_C(\omega) = \eta(\omega) V_S(\omega), \quad (5)$$

where $\eta(\omega) = 1/[i\omega C_G(2R_G + mR_0) + 1]$ denotes the efficiency of the loading voltage. The normalized modulation voltage as a function of small-signal frequency is shown in Fig. 4(b). Combining the curves in Figs. 4(a) and 4(b), the modulation depth as a function of the frequency ω is shown in Fig. 4(c). The result gives the 3-dB cutoff frequency around 50 GHz, which is much larger than the typical modulation speed of graphene absorption modulators [41] (see Sec. S4 of the Supplemental Material for details [26]). Also, the 7-dB cutoff frequency is over 30 GHz, which enables on-chip high-data-rate interconnects and high-sensitivity sensing applications.

Figures 4(d)–4(g) show the energy flow in the y direction for different cases (see Sec. S3 of the Supplemental Material for 3D simulation details [26]). As shown in Figs. 4(d) and 4(e), the energy is concentrated in the air gap when the modulator is at the on state, which leads to low loss and long propagation distance. However, the propagation energy decays rapidly when the modulator is switched to the off state, as shown in Figs. 4(f) and 4(g). Part of the energy is reflected by the interface, and the rest is diffused and absorbed. In order to achieve higher modulation efficiency, it is necessary to destroy the long-propagation mode as much as possible within the limited modulation length. Thus, two modulation regions connected in series are applied as explained above, separated by a 350-nm type-II buffer region, and the length of each modulation region is 30 nm.

VI. DISCUSSION AND CONCLUSION

It is emphasized that one of the main factors affecting the modulation speed is the quality of electrical contacts quantified by contact resistance, which should be as small as possible. Many technologies have proved to be effective for reducing the contact resistance, including increasing the contact areas and adopting edge contact and seamless electrical contacts [42]. Furthermore, the modulation depth

can be increased by cascading more modulation regions together with the buffer regions; however, their fabrication process may be complicated. In terms of the potential fabrication process, the HMM2Ds can be realized by layer-by-layer transfer [43] of a 2D graphene- h -BN nanoribbon, which is prepared using heteroepitaxial growth [44]. The chemical doping of graphene can be executed by the substitution of one or several carbon atoms in the graphene lattice by other chemical elements such as nitrogen or boron atoms [45] in the growth process. The rest of the fabrication of the HMM2D modulator would be well integrated with micro-nano processing, including electron beam lithography and film deposition that are compatible with the standard CMOS technology. On the other hand, the proposed HMM2Ds can be extended to phase modulators [46] for realizing more complicated modulation function. And due to the rich tunable properties of graphene, the device can be tuned by optical illumination as well, which would possibly provide a modulation speed into the terahertz region. Last but not least, other physical phenomena and optoelectronic properties observed in graphene- h -BN heterostructures, such as the quantum Hall effect [47], would enable design principles for optoelectronic devices, for example, an optical modulator based on a magnetic field.

In conclusion, we demonstrate a high-speed, efficient, and compact on-chip EO modulator working at MIR wavelengths based on HMM2Ds. The modulation performance is evaluated by several key figures of merit, including the operating bandwidth, propagation loss, modulation depth, and speed. The proposed device working at 5 μm gives a maximum modulation depth of 30 dB and the 3-dB modulation speed reaches up to 50 GHz based on the small-signal frequency-response model. The low-loss plasmonic gap-mode design makes possible nanoscale compactness and high energy efficiency. Also, the proposed HMM2Ds can be integrated with other 2D fluorescence materials straightforwardly, paving the way towards an integrated MIR PICs platform for efficient on-chip information processing.

ACKNOWLEDGMENTS

The work at Zhejiang University is sponsored by the National Natural Science Foundation of China (NNSFC) under Grant No. 62005237.

H.Q. conceived the idea. D.L. conducted the numerical simulations. D.L., H.M., and H.Q. contributed extensively to the writing of the manuscript. All the authors analyzed data and interpreted the details of the results. W.Y., H.C., and H.Q. supervised the research.

- [1] R. Soref, Mid-infrared photonics in silicon and germanium, *Nat. Photonics* **4**, 495 (2010).

- [2] S.-S. Kim, C. Young, and B. Mizaikoff, Miniaturized mid-infrared sensor technologies, *Anal. Bioanal. Chem.* **390**, 231 (2008).
- [3] Z. Chen, T. W. Hänsch, and N. Picqué, Mid-infrared feed-forward dual-comb spectroscopy, *Proc. Natl Acad. Sci. USA* **116**, 3454 (2019).
- [4] A. J. Lind, A. Kowligy, H. Timmers, F. C. Cruz, and S. A. Diddams, Mid-Infrared Frequency Comb Generation and Spectroscopy with Few-Cycle Pulses and $\chi^{(2)}$ Nonlinear Optics, *Phys. Rev. Lett.* **124**, 133904 (2020).
- [5] H. Ren, L. Shen, A. F. J. Runge, T. W. Hawkins, J. Ballato, U. Gibson, and A. C. Peacock, Low-loss silicon core fibre platform for mid-infrared nonlinear photonics, *Light Sci. Appl.* **8**, 105 (2019).
- [6] S. D. Jackson, Towards high-power mid-infrared emission from a fibre laser, *Nat. Photonics* **6**, 423 (2012).
- [7] C. Chen, F. Chen, X. Chen, B. Deng, B. Eng, D. Jung, Q. Guo, S. Yuan, K. Watanabe, and T. Taniguchi, Bright mid-infrared photoluminescence from thin-film black phosphorus, *Nano Lett.* **19**, 1488 (2019).
- [8] C. Chen, X. Lu, B. Deng, X. Chen, Q. Guo, C. Li, C. Ma, S. Yuan, E. Sung, and K. Watanabe, Widely tunable mid-infrared light emission in thin-film black phosphorus, *Sci. Adv.* **6**, eaay6134 (2020).
- [9] X. Zong, H. Hu, G. Ouyang, J. Wang, R. Shi, L. Zhang, Q. Zeng, C. Zhu, S. Chen, and C. Cheng, Black phosphorus-based van der Waals heterostructures for mid-infrared light-emission applications, *Light Sci. Appl.* **9**, 1 (2020).
- [10] L. Huang, B. Dong, X. Guo, Y. Chang, N. Chen, X. Huang, W. Liao, C. Zhu, H. Wang, and C. Lee, Waveguide-integrated black phosphorus photodetector for mid-infrared applications, *ACS Nano* **13**, 913 (2018).
- [11] B. Schwarz, P. Reininger, D. Ristanić, H. Detz, A. M. Andrews, W. Schrenk, and G. Strasser, Monolithically integrated mid-infrared lab-on-a-chip using plasmonics and quantum cascade structures, *Nat. Commun.* **5**, 4085 (2014).
- [12] A. G. Griffith, R. K. Lau, J. Cardenas, Y. Okawachi, A. Mohanty, R. Fain, Y. H. D. Lee, M. Yu, C. T. Phare, and C. B. Poitras, Silicon-chip mid-infrared frequency comb generation, *Nat. Commun.* **6**, 1 (2015).
- [13] M. Yu, Y. Okawachi, A. G. Griffith, N. Picqué, M. Lipson, and A. L. Gaeta, Silicon-chip-based mid-infrared dual-comb spectroscopy, *Nat. Commun.* **9**, 1869 (2018).
- [14] Y. Wu, Z. Qu, A. Osman, W. Cao, A. Z. Khokhar, J. Soler Penades, O. L. Muskens, G. Z. Mashanovich, and M. Nedeljkovic, Mid-infrared nanometallic antenna assisted silicon waveguide based bolometers, *ACS Photonics* **6**, 3253 (2019).
- [15] D. Marpaung, J. Yao, and J. Capmany, Integrated microwave photonics, *Nat. Photonics* **13**, 80 (2019).
- [16] I. M. Sopko, D. O. Ignatyeva, G. A. Knyazev, and V. I. Belotelov, Efficient Acousto-Optical Light Modulation at the Mid-Infrared Spectral Range by Planar Semiconductor Structures Supporting Guided Modes, *Phys. Rev. Appl.* **13**, 034076 (2020).
- [17] I. M. Sopko and G. A. Knyazev, Plasmonic enhancement of mid- and far-infrared acousto-optic interaction [invited], *Appl. Opt.* **57**, C42 (2018).
- [18] J. Chiles and S. Fathpour, Mid-infrared integrated waveguide modulators based on silicon-on-lithium-niobate photonics, *Optica* **1**, 350 (2014).
- [19] R. Peng, K. Khaliji, N. Youngblood, R. Grassi, T. Low, and M. Li, Midinfrared electro-optic modulation in few-layer black phosphorus, *Nano Lett.* **17**, 6315 (2017).
- [20] Z. Sun, A. Martinez, and F. Wang, Optical modulators with 2D layered materials, *Nat. Photonics* **10**, 227 (2016).
- [21] B. Sensale-Rodriguez, R. Yan, M. M. Kelly, T. Fang, K. Tahy, W. S. Hwang, D. Jena, L. Liu, and H. G. Xing, Broadband graphene terahertz modulators enabled by intraband transitions, *Nat. Commun.* **3**, 1 (2012).
- [22] M. Liu, X. Yin, E. Ulin-Avila, B. Geng, T. Zentgraf, L. Ju, F. Wang, and X. Zhang, A graphene-based broadband optical modulator, *Nature* **474**, 64 (2011).
- [23] Y. Yao, R. Shankar, M. A. Kats, Y. Song, J. Kong, M. Loncar, and F. Capasso, Electrically tunable metasurface perfect absorbers for ultrathin mid-infrared optical modulators, *Nano Lett.* **14**, 6526 (2014).
- [24] C. R. Dean, A. F. Young, I. Meric, C. Lee, L. Wang, S. Sorgenfrei, K. Watanabe, T. Taniguchi, P. Kim, K. L. Shepard, *et al.*, Boron nitride substrates for high-quality graphene electronics, *Nat. Nanotechnol.* **5**, 722 (2010).
- [25] J. Xue, J. Sanchez-Yamagishi, D. Bulmash, P. Jacquod, A. Deshpande, K. Watanabe, T. Taniguchi, P. Jarillo-Herrero, and B. J. LeRoy, Scanning tunnelling microscopy and spectroscopy of ultra-flat graphene on hexagonal boron nitride, *Nat. Mater.* **10**, 282 (2011).
- [26] See Supplemental Material at <http://link.aps.org/supplemental/10.1103/PhysRevApplied.16.034002> for more information regarding the electrode scheme, mode discussion, simulation details, and performance metrics.
- [27] S. Srivastava, H. Kino, and C. Joachim, Contact conductance of a graphene nanoribbon with its graphene nanoelectrodes, *Nanoscale* **8**, 9265 (2016).
- [28] X. Luo, T. Qiu, W. Lu, and Z. Ni, Plasmons in graphene: Recent progress and applications, *Mater. Sci. Eng. R Rep.* **74**, 351 (2013).
- [29] A. Woessner, M. B. Lundeberg, Y. Gao, A. Principi, P. Alonso-González, M. Carrega, K. Watanabe, T. Taniguchi, G. Vignale, M. Polini, *et al.*, Highly confined low-loss plasmons in graphene–boron nitride heterostructures, *Nat. Mater.* **14**, 421 (2015).
- [30] B. Scharf, V. Perebeinos, J. Fabian, and P. Avouris, Effects of optical and surface polar phonons on the optical conductivity of doped graphene, *Phys. Rev. B* **87**, 035414 (2013).
- [31] A. Laturia, M. L. Van de Put, and W. G. Vandenberghe, Dielectric properties of hexagonal boron nitride and transition metal dichalcogenides: From monolayer to bulk, *npj 2D Mater. Appl.* **2**, 6 (2018).
- [32] S. Dai, Z. Fei, Q. Ma, A. S. Rodin, M. Wagner, A. S. McLeod, M. K. Liu, W. Gannett, W. Regan, K. Watanabe, *et al.*, Tunable phonon polaritons in atomically thin van der Waals crystals of boron nitride, *Science* **343**, 1125 (2014).
- [33] Y. Cai, L. Zhang, Q. Zeng, L. Cheng, and Y. Xu, Infrared reflectance spectrum of BN calculated from first principles, *Solid State Commun.* **141**, 262 (2007).
- [34] S. Dai, Q. Ma, M. Liu, T. Andersen, Z. Fei, M. Goldflam, M. Wagner, K. Watanabe, T. Taniguchi, and M. Thiemens,

- Graphene on hexagonal boron nitride as a tunable hyperbolic metamaterial, *Nat. Nanotechnol.* **10**, 682 (2015).
- [35] M. N. Gjerding, R. Petersen, T. G. Pedersen, N. A. Mortensen, and K. S. Thygesen, Layered van der Waals crystals with hyperbolic light dispersion, *Nat. Commun.* **8**, 1 (2017).
- [36] A. Chebykin, A. Orlov, C. Simovski, Y. S. Kivshar, and P. A. Belov, Nonlocal effective parameters of multilayered metal-dielectric metamaterials, *Phys. Rev. B* **86**, 115420 (2012).
- [37] C. Haffner, D. Chelladurai, Y. Fedoryshyn, A. Josten, B. Baeuerle, W. Heni, T. Watanabe, T. Cui, B. Cheng, S. Saha, *et al.*, Low-loss plasmon-assisted electro-optic modulator, *Nature* **556**, 483 (2018).
- [38] I. Dolado, F. J. Alfaro-Mozaz, P. Li, E. Nikulina, A. Bylinkin, S. Liu, J. H. Edgar, F. Casanova, L. E. Hueso, P. Pablo Alonso-González, *et al.*, Nanoscale guiding of infrared light with hyperbolic volume and surface polaritons in van der Waals material ribbons, *Adv. Mater.* **32**, 1906530 (2020).
- [39] G. T. Reed, G. Mashanovich, F. Y. Gardes, and D. J. Thomson, Silicon optical modulators, *Nat. Photonics* **4**, 518 (2010).
- [40] L. Wang, I. Meric, P. Y. Huang, Q. Gao, Y. Gao, H. Tran, T. Taniguchi, K. Watanabe, L. M. Campos, D. A. Muller, *et al.*, One-dimensional electrical contact to a two-dimensional material, *Science* **342**, 614 (2013).
- [41] C. T. Phare, Y.-H. Daniel Lee, J. Cardenas, and M. Lipson, Graphene electro-optic modulator with 30 GHz bandwidth, *Nat. Photonics* **9**, 511 (2015).
- [42] A. Allain, J. Kang, K. Banerjee, and A. Kis, Electrical contacts to two-dimensional semiconductors, *Nat. Mater.* **14**, 1195 (2015).
- [43] K. Kang, K.-H. Lee, Y. Han, H. Gao, S. Xie, D. A. Muller, and J. Park, Layer-by-layer assembly of two-dimensional materials into wafer-scale heterostructures, *Nature* **550**, 229 (2017).
- [44] L. Liu, J. Park, D. A. Siegel, K. F. McCarty, K. W. Clark, W. Deng, L. Basile, J. C. Idrobo, A.-P. Li, and G. Gu, Heteroepitaxial growth of two-dimensional hexagonal boron nitride templated by graphene edges, *Science* **343**, 163 (2014).
- [45] F. Joucken, L. Henrard, and J. Lagoute, Electronic properties of chemically doped graphene, *Phys. Rev. Materials* **3**, 110301 (2019).
- [46] V. Soriano, M. Midrio, G. Contestabile, I. Asselberghs, J. Van Campenhout, C. Huyghebaert, I. Goykhman, A. K. Ott, A. C. Ferrari, and M. Romagnoli, Graphene-silicon phase modulators with gigahertz bandwidth, *Nat. Photonics* **12**, 40 (2018).
- [47] M. Yankowitz, Q. Ma, P. Jarillo-Herrero, and B. J. LeRoy, Van der Waals heterostructures combining graphene and hexagonal boron nitride, *Nat. Rev. Phys.* **1**, 112 (2019).